Letter

Chemical strain induced Rashba effect in two-dimensional Ruddlesden-Popper perovskites

Suhas K. T.[1], Tisita Das[2], Aditya Singh[3], Azat Khadiev[4], Ajay Soni[3], Sudip Chakraborty[2], and Ranjani Viswanatha[5,6,*]

[1]*Chemistry and Physics of Materials Unit, Jawaharlal Nehru Centre for Advanced Scientific Research, Jakkur, Bangalore 560064, India*
[2]*Materials Theory for Energy Scavenging (MATES) Lab, Harish Chandra Research Institute (HRI) Allahabad, AC.I. of Homi Bhabha National Institute (HBNI), Prayagraj (Allahabad), U.P. 211019, India*
[3]*School of Physical Sciences, Indian Institute of Technology Mandi-175005 Himachal Pradesh, India*
[4]*Deutsches Elektronen-Synchrotron DESY, Notkestr. 85, 22607 Hamburg, Germany*
[5]*New Chemistry Unit, Jawaharlal Nehru Centre for Advanced Scientific Research, Jakkur, Bangalore 560064, India*
[6]*International Centre for Materials Science, Jawaharlal Nehru Centre for Advanced Scientific Research, Jakkur, Bangalore 560064, India*

(Received 27 August 2024; revised 12 December 2024; accepted 14 January 2025; published 3 February 2025)

We report the observation of Rashba splitting in multilayer $Cs_2PbI_2Cl_2$ two-dimensional Ruddlesden-Popper phase perovskite nanocrystals (NCs) induced by chemical strain. Magnetic circular dichroism measurements reveal significant Zeeman splitting, indicating strong spin-orbit coupling. At 10 K, pronounced circular dichroism signals suggest structural asymmetry linked to the Rashba effect. Photoluminescence (PL) peak splitting at low temperatures, supported by polarization-dependent PL measurements showing emission anisotropy below 70 K, confirms the presence of spin selectivity. High-resolution synchrotron x-ray diffraction and temperature-dependent Raman data reveal a transition in unit cell parameters and phonon frequencies around 70 K, respectively, correlating with optical data. The strain induced local asymmetry facilitates these effects. Density functional theory calculations validate the experimental findings, showing clear spin splitting in the valence and conduction bands. This study investigates the influence of chemical strain on asymmetry-induced phenomena, such as the Rashba effect in $Cs_2PbI_2Cl_2$ NCs, highlighting their potential as a promising platform for advanced technologies.

DOI: 10.1103/PhysRevB.111.L081401

Quantum electronic effects such as valleytronics and Rashba splitting have attracted significant attention due to their potential in next-generation electronic and optoelectronic devices [1–4]. Rashba effect, where charge carriers (electrons and holes) are selectively populated in specific energy valleys of a material's electronic band structure, is key to this field [1,5–7]. Like spintronics, where information is encoded in electron spin [2], valleytronics leverages these valleys for information processing and storage. Polarization can be controlled using optical pumping with circularly polarized light [8], strain [9–11], and external magnetic fields [12–16], opening unique possibilities for valley-based transistors, quantum computing, and optoelectronics with valley-specific emission properties [17–21]. Additionally, spin-valley coupling can enhance the lifetime of spin-valley polarization [22] and enable selective spin manipulation within the valley [23]. The Rashba effect, arising from significant spin-orbit coupling (SOC) [24,25] and broken inversion symmetry, leads to spin splitting in electronic bands, facilitating spin control through circularly polarized light [8]. Notably, strong Rashba spin splitting in two-dimensional (2D) Ruddlesden-Popper perovskites [26–29] and strongly coupled spin-valley physics in monolayer transition metal dichalcogenides (TMDs) introduce spin-valley-dependent optical selection rules to the interlayer excitons present in the heterostructure of these 2D Ruddlesden-Popper phase (RPP) and monolayer TMDs [4].

Monolayers of 2D TMDs such as MoS_2, $MoSe_2$, WS_2, and WSe_2, are ideal for observing quantum electronic effects due to their multiple equivalent energy minima (valleys) in their conduction or valence bands [30,31]. With strong SOC, the time-reversal symmetry causes opposing spin splitting at the $+K$ and $-K$ valleys, linking spin and valley pseudospin [23]. A key requirement for these effects is the lack of inversion symmetry, which leads to different optical transition rules in different valleys [32,33]. However, challenges such as complex large-scale production, limited material options, and high costs hinder their application. This work proposes an approach to overcome these limitations by introducing large chemical strains to prevent interlayer interaction, thus eliminating the effect of inversion symmetry. We tested this on $Cs_2PbI_2Cl_2$ nanocrystals, where the significant size difference between Cl^- and I^- creates strain that structurally separates the layers. At low temperatures, this strain prevents interlayer interaction, allowing us to observe effects typically hindered by such interactions.

In this study, we used atomic force microscopy (AFM) to determine the number of monolayers of $Cs_2PbI_2Cl_2$. We then demonstrated Rashba spin splitting through temperature-dependent photoluminescence (PL) and circular dichroism (CD) measurements. At low temperatures (10–70 K), PL peak splitting and strong CD signals supported our

*Contact author: rv@jncasr.ac.in

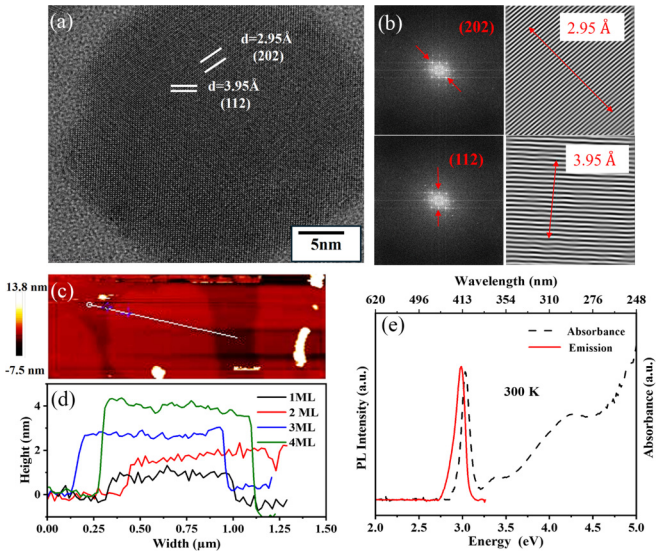

FIG. 1. (a) HRTEM image and (b) HRTEM analysis of $Cs_2PbI_2Cl_2$ NPLs. (c) AFM image of $Cs_2PbI_2Cl_2$. (d) Line-scan data of the AFM image. (e) Room temperature absorbance and emission of $Cs_2PbI_2Cl_2$ NPLs.

hypotheses. High-resolution synchrotron x-ray diffraction (XRD) and temperature-dependent Raman measurements revealed distinct transitions in unit cell parameters, Pb-Cl bond length, and phonon frequencies below 75 K, respectively, aligning with the observed optical transitions. Magnetic circular dichroism (MCD) studies indicated strong spin-orbit coupling, while density functional theory (DFT) calculations confirmed spin splitting at the band extrema. Our work provides a comprehensive exploration of spin-valley physics in all-inorganic 2D perovskites, marking chemical strain as a parameter to tune the Rashba effect in these materials.

$Cs_2PbI_2Cl_2$ nanoplatelets were synthesized by injecting mixed olylammonium halide salts, followed by rapid cooling [34]. A brief synthesis protocol is included in the Supplemental Material [35].

High resolution transmission electron microscopy (HRTEM) images and selected area electron diffraction patterns of $Cs_2PbI_2Cl_2$ nanostructures [Figs. 1(a) and 1(b)], confirm the formation of platelets, predominantly exhibiting (110), (202), and (303) planes along the [001] axis. This suggests horizontal packing of $[PbI_2Cl_4]^{4-}$ layers within the flat platelet structure. Monolayers of 2D materials inherently lack inversion symmetry, making monolayer coverage without the interference of multilayer stacking crucial for observing quantum effects like Rashba spin splitting and valley polarization. Hence the presence of multilayer stacking negates the advantage of lacking inversion symmetry, significantly altering their electronic properties [36]. A typical AFM area [Fig. 1(c)] and line-scan analysis [Fig. 1(d)] show nanoplatelet thicknesses ranging from 1 to 4 nm, corresponding to 1 to 5 monolayers. This is not surprising as the colloidal synthesis and spin-coating process facilitates the ease of sample preparation but does not allow precise control over layer thickness. Further, the inversion symmetry breaking observed in single monolayers of TMDs is absent due to the presence of multiple monolayers.

Optical spectroscopy reveals that these 1–5-nm-thick nanocrystals with ∼60 nm lateral dimensions exhibit strongly confined excitonic absorption [indicated by the black dashed line in Fig. 1(e)], attributed to the separation of Pb-Cl layers, causing quantum confinement along the z axis. The narrow excitonic absorption peak at 3.047 eV (407 nm) aligns with the reported 3.04 eV band gap [37]. The sharp emission peak at 2.99 eV at room temperature [red solid line in Fig. 1(e)] corresponds to band edge emission.

XRD data [Fig. 2(a)] and Rietveld analysis (Supplemental Material Fig. S1) of nanoplatelets at 300,70, and 5 K reveals that $Cs_2PbI_2Cl_2$ crystallizes in the 2D RPP structure with the $I4/mmm$ space group, akin to the K_2NiF_4-type structure, featuring corner-sharing $[PbI_2Cl_4]^{4-}$ octahedral layers. The Cl^- ions occupy the equatorial positions and I^- ions occupy the axial sites. The sharper peaks in the $xy0$ plane family [Fig. 2(a)], suggest anisotropic growth, indicating the nanocrystals (NCs) are primarily composed of stacked $[PbI_2Cl_4]^{4-}$ octahedral layers, electrically balanced by Cs^+ counterions.

To understand the dynamics of $Cs_2PbI_2Cl_2$, we performed temperature-dependent XRD, collecting high-resolution synchrotron data between 5 and 300 K [Fig. 2(a)]. The zoomed area [Fig. 2(b)] shows minimal peak shifts from 5 to 70 K, but a gradual shift occurs between 70 and 300 K. Rietveld refinement [Supplemental Material Fig. S1 and Tables I(a) and I(b)] confirms that the overall crystal structure ($I4/mmm$) remains unchanged across all temperatures. However, a transition is evident, as seen in the changes in unit cell parameters: $\Delta a = \Delta b = 0.03521(7)$ Å, $\Delta c = 0.21530(62)$ Å, and $\Delta V = 14.4$ Å^3 at 5 K compared to 300 K. The cell parameters [Supplemental Material Figs. S2(a)–S2(c)] remain stable from 5 to 70 K but increase rapidly from 70 to 300 K, suggesting a transition near ∼70 K that may introduce local asymmetry, influencing optical properties.

To explore the origin of the observed transition and the role of involved phonons, we performed temperature-dependent Raman spectroscopy between 3 and 300 K. At 3 K, the Raman spectra of $Cs_2PbI_2Cl_2$ revealed four prominent modes at 26.3 (E_g), 48.5 (E_g), 57 (A_{1g}), and 93.2 cm^{-1} (A_{1g}) [Fig. 2(c)] [37,38]. The evolution of these modes, particularly the A_{1g} (93 cm^{-1}) mode, was tracked across the temperature range [Fig. 2(d)]. A transition around 75 K was observed [Fig. 2(d) and Figs. S2(d)–S2(g)], which aligns with the changes in unit cell parameters near 70 K seen in the XRD data, indicating a structural transition at low temperatures.

Optical studies as a function of temperature were carried out to understand the structural transition. Figure 3(a) displays a typical absorbance spectrum at 10 K while the CD signal at 10 and 300 K is shown in the inset (I) of Fig. 3(b). At room temperature (300 K) the sample exhibits no detectable CD signal, indicating the absence of inversion symmetry. In contrast, at 10 K, the figure reveals a pronounced CD signal. This CD signal at 10 K originates predominantly from the band edge, with minor contributions from transitions at higher energy states. The presence of a nonzero CD signal indicates structural chirality or asymmetry, resulting in differential absorption of left and right circularly polarized light. The robust

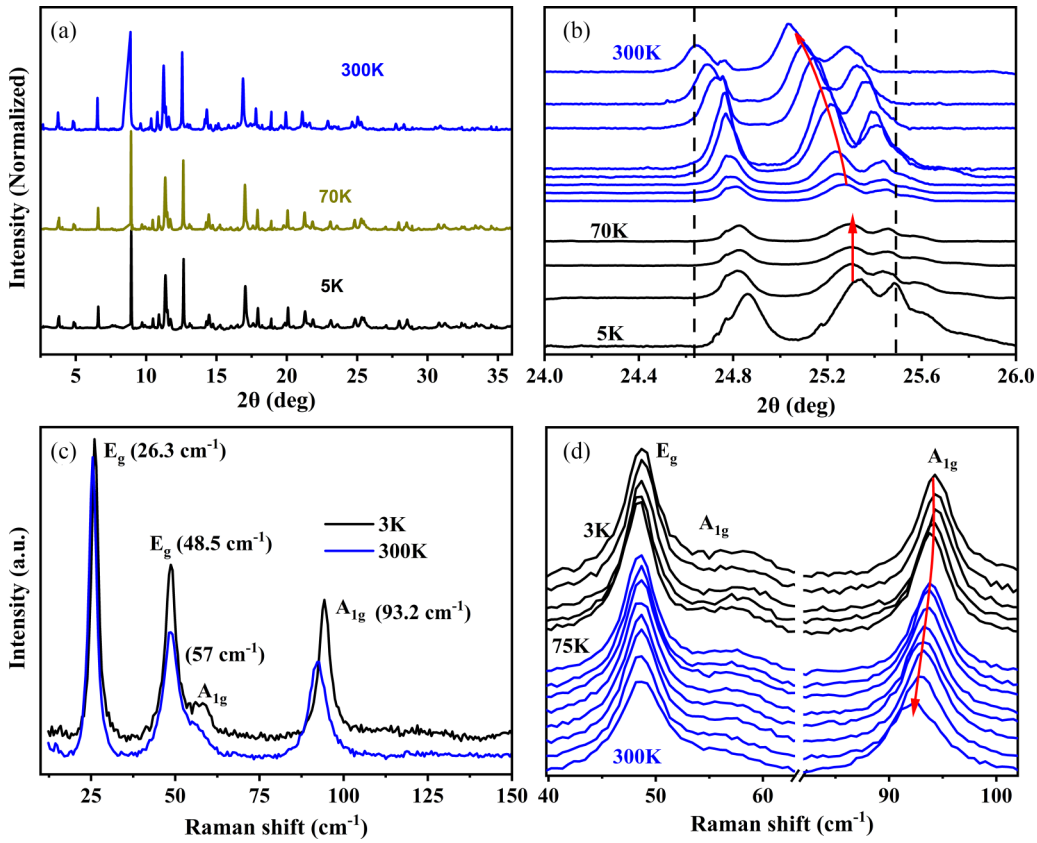

FIG. 2. (a) Synchrotron XRD data of $Cs_2PbI_2Cl_2$ at 300, 70, and 5 K. (b) Temperature-dependent synchrotron XRD shows the shift in the peak positions above 70 K. (c) Raman peak comparison between 3 and 300 K. (d) Temperature-dependent Raman spectra showing transition around 75 K supporting the XRD data.

CD signal at low temperature in 2D $Cs_2PbI_2Cl_2$ highlights the pronounced structural asymmetry in this material, despite the absence of monolayer geometry.

To further investigate the impact of structural characteristics and transitions in this temperature range, particularly inversion symmetry breaking, we synthesized Cs_2PbI_2BrCl nanoplatelets. The formation of Cs_2PbI_2BrCl was confirmed using XRD and HRTEM, as shown in Figs. S3(a) and S3(b) in the Supplemental Material. CD measurements conducted at 10 K on this sample revealed the absence of a CD signal [inset (II) of Fig 3(b)] suggesting that this effect is unique to $Cs_2PbI_2Cl_2$. Detailed understanding through the structural analysis of these two samples reveals that substituting Br^- for Cl^- reduces the anion size disparity in Cs_2PbI_2BrCl, resulting in enhanced interlayer interactions. This reduction in interplanar distances was confirmed through interplanar spacing calculations from HRTEM data and the XRD Rietveld refinement (Supplemental Material Table II). Thus, the substitution reduces the chemical strain compared to the I^-/Cl^- combination, suggesting that the strain could play a critical role in the observed asymmetry.

Further, in the presence of a magnetic field, the CD signal intensifies significantly, as illustrated in Fig. 3(b). The Zeeman splitting (E_Z), calculated using $\Delta E_Z = -(\sqrt{(e}/2) * \sigma * (\Delta A/A)$, is notably greater than that observed in three-dimensional $CsPb(Br_{0.4}Cl_{0.6})_3$ perovskites with a similar band gap [see Fig. 3(b), inset (III) and Fig. S4 of the Supplemental Material]. This substantial difference suggests significant spin-orbit coupling in $Cs_2PbI_2Cl_2$, attributable to its 2D structure and the presence of Pb. Enhanced Zeeman splitting is crucial for spintronics, allowing precise control of electron spins. To further explore the magnetic field dependence and asymmetry effects, we obtained MCD spectra at $+5$ and -5 T, shown in Fig. 3(c). The spectra do not reverse symmetrically, indicating the asymmetric nature of the Zeeman splitting. The difference spectrum, plotted at the bottom of Fig. 3(c), reveals distinct variations in the MCD spectra.

The robust CD signal in the 2D RPP structure of $Cs_2PbI_2Cl_2$, along with significant spin-orbit coupling, led us to explore the possibility of the Rashba effect in this material. The CD signal observed at lower temperatures indicates a transition from symmetric to asymmetric behavior below 60 K. To investigate valley polarization and optical anisotropy, we performed polarization-resolved PL measurements from 13 to 300 K. Figure S5 shows the temperature-dependent PL spectra of $Cs_2PbI_2Cl_2$. At room temperature, a broad peak at $\sim$2.99 eV, associated with the band edge, is observed. Below 70 K, this peak splitting shows a shoulder at around 2.94 eV (Fig. S5). This peak splitting, observed at $\sim$2.83 and $\sim$2.94 eV, suggests the presence of different valleys due to valley polarization.

We used computer-controlled polarizing prisms to measure polarization-resolved emission intensity across four configurations: 0°-0° (V-V), 0°-90° (V-H), 90°-90° (H-H), and 90°-0° (H-V). Details of these measurements are provided

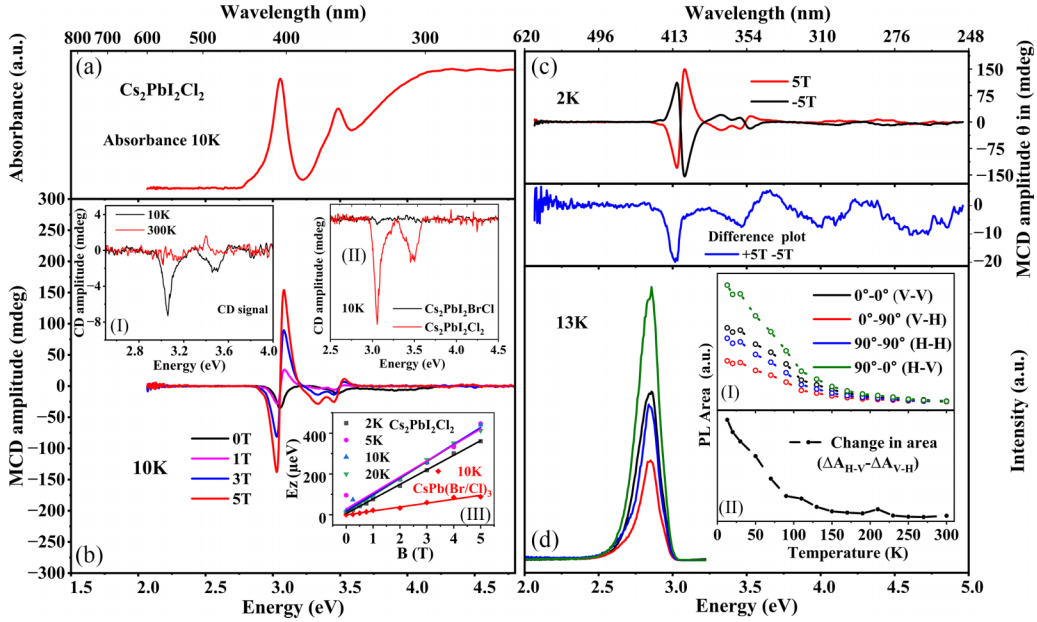

FIG. 3. (a) Absorbance spectra of $Cs_2PbI_2Cl_2$ at 10 K. (b) MCD spectra of $Cs_2PbI_2Cl_2$ at 10 K with increasing magnetic field from 0 to 5 T. Inset (I) shows the absence of CD signal at room temperature and a strong CD signal at 10 K. Inset (II) shows the absence of CD signal in Cs_2PbI_2BrCl at 10 K while inset (III) shows a comparison of the Zeeman energy of $Cs_2PbI_2Cl_2$ with $CsPb(Br/Cl)_3$ NCs. (c) MCD signal showing a lack of exact peak reversal upon reversing the magnetic field. The difference spectrum shown in the bottom of (c) indicates the anisotropic nature of the sample. (d) Anisotropic PL emission at 13 K. Inset (I) shows temperature-dependent variation of the area under the curve. Inset (II) shows the difference in PL area between the two different polarization directions.

in the supporting information, and the corresponding plots are provided in Fig. 3(d). We observed a clear directional dependence in emission intensities: V-V and H-H configurations showing similar intensities, while the intensity peaked in the H-V configuration and minimized in V-H, indicating anisotropic emission. The temperature-dependent valley polarization is shown as the difference in area under the curve for H-V and V-H in the inset of Fig. 3(d). This area difference remains nearly constant from 300 to 90 K but increases significantly below 70 K, suggesting a significant asymmetry below this temperature. The energy difference between split PL peaks corresponds to the valley energy separation, with greater splitting indicating larger separations.

These properties are substantially influenced by factors such as crystal lattice structure, spin-orbit coupling, and electron-electron interactions [39]. At elevated temperatures (>70 K), thermal energy allows electrons to occupy multiple states, resulting in broad PL peaks. Below 70 K, thermal energy is insufficient to overcome intervalley barriers, confining electrons to certain regions of the energy landscape. This confinement causes PL to be emitted from individual valleys, leading to a peak splitting into distinct energies (2.83 and 2.94 eV in Fig. S5).

At elevated temperatures, thermal energy excites electrons to higher energy states, potentially filling both spin-split bands caused by the Rashba effect. Consequently, electrons may occupy multiple states with distinct energy levels, leading to broad photoluminescence peaks around ∼2.83 eV, as observed in PL polarization studies. As the temperature decreases, thermal energy diminishes, causing electrons to localize in specific valleys, particularly those with lower energy levels influenced by the Rashba effect. This selective localization results in PL emission from specific valleys, each associated with a unique valley and spin state.

In materials like TMDs, the Rashba effect can manifest as variations in PL intensity or peak energy based on excitation and emission polarization, a trend also observable in temperature-dependent CD measurements. Figure 4(a) shows that the CD amplitude decreases after 60 K. To link optical asymmetry with structural asymmetry, we used VESTA software to analyze atomic positions in the a and b directions. We found that Pb-Cl bonds align along both axes and calculated their bond lengths. Temperature mapping of Pb-Cl bond lengths reveals a significant transition around ∼70 K [Fig. 4(b)], correlating with the PL and CD transitions. This suggests that the transition is linked to valley polarization and Rashba splitting in the material.

To investigate the strain dependence of crystal structure, we analyzed synchrotron XRD data collected from 3 to 300 K to determine the lattice strain, employing the Williamson-Hall equation, $\beta\cos\theta = \varepsilon(4\sin\theta) + (K\lambda/D)$ [40]. Here, β is the integral breadth of the XRD reflection, D is the crystallite size, K is the shape factor (≈0.9), λ is the x-ray wavelength, ε is the lattice strain, and θ is Bragg's angle. The Williamson-Hall plots are shown in Fig. S6. The strain values (ε) plotted against temperature in Fig. 4(c) reveal a significant increase below 70 K. This rise in lattice strain likely reduces crystallinity and induces local asymmetry in the crystal structure. Such strain induced effects can alter the band structure and spin-orbit interaction, enhancing the Rashba effect. Below 70 K, the strain enhances local asymmetry and facilitates Rashba splitting within the system.

The phonon frequency versus temperature plot highlights thermal (strain) relaxation above 75 K [Figs. S2(d)–S2(g)].

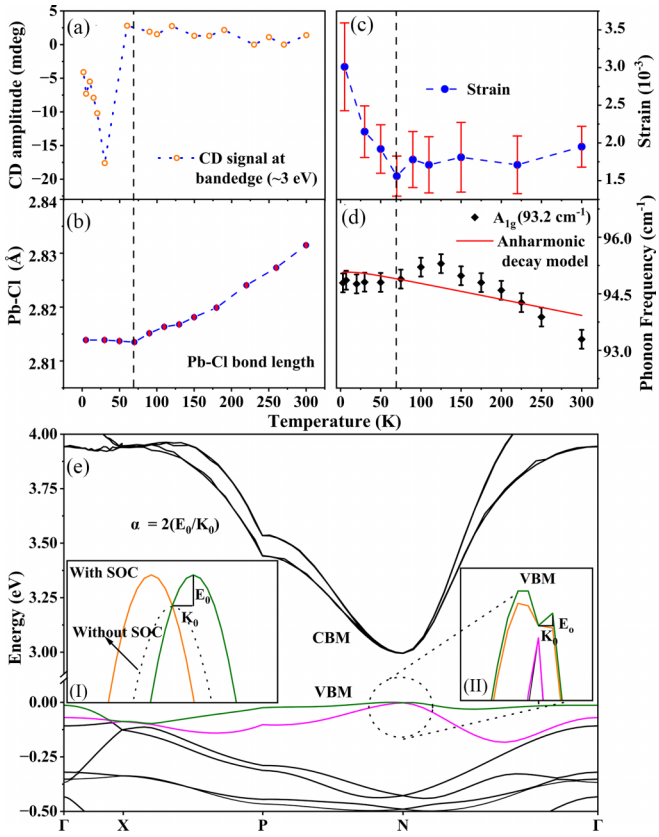

FIG. 4. (a) Variation of CD signal amplitude with the temperature. (b) Variation of Pb-Cl bond length with the temperature. (c) Variation of strain as a function of temperature. (d) The phonon frequency of the A_{1g} mode as a function of temperature along with the fit obtained for the anharmonic decay model. (e) Valence band maxima (VBM) and the conduction band minimum (CBM) from the band structure calculation. Inset (I) shows the schematic of the Rashba effect and inset (II) shows the zoomed area of the VBM.

As temperature decreases from 300 to 125 K, a systematic hardening of phonon frequencies is observed, as expected. However, between 125 and 75 K, we noted anomalous behavior where Raman modes exhibit softening, likely due to tensile strain. Below 75 K, the Raman modes stabilize, neither softening nor hardening, correlating with the increased strain observed in the XRD data [Figs. 4(c) and 4(d)].

The phonon frequency analysis using the anharmonic decay model [Fig. 4(d)] shows the frequency can be modeled as $\omega(T) = \omega_0 - \frac{A}{e^{\frac{\hbar\omega_0}{2k_BT}}-1}$ where $\omega(T)$, ω_0 are the phonon frequencies at temperature T and at 0 K, respectively, and A is the anharmonic constant. The estimated A values from the model are ~0.22 cm^{-1} (E_g), ~0.20 cm^{-1} (A_{1g}), and ~0.29 cm^{-1} (A_{1g}). The significant deviation of the A_{1g} (93.2 cm^{-1}) mode from the anharmonic model around 75 K [Fig. 4(d)] indicates stronger electron-phonon coupling. The phonon lifetime (τ_i) for the A_{1g} (93.2 cm^{-1}) mode obtained from the equation $\tau_i = \frac{1}{2\pi c(\mathrm{FWHM})_i}$ was found to range from 1.5 to 2.4 ps, further emphasizing the material's high crystalline anharmonicity. The anomalous softening of the A_{1g} (93.2 cm^{-1}) modes not only indicates the development of tensile strain but also suggests a significant deviation from the anharmonic decay model [as shown in Fig. 4(d)]. Such deviations are often reported in materials undergoing structural transitions or exhibiting spin-phonon coupling [41].

In order to validate the experimental signature of Rashba splitting in 2D $Cs_2PbI_2Cl_2$ NCs, we performed first-principles electronic structure calculations within the framework of DFT formalism. The NCs were found to be simulated in a tetragonal phase, consistent with experimental observations [Fig. S7(a)]. The calculated band gap through DFT calculations is 2.99 eV, which is in good agreement with experimental observation, as the sharp emission peak observed corresponds to experimental band edge emission as depicted in Fig. 1(e). The band structure analysis [Fig. 4(e)] revealed Rashba-like splitting at both the valence band maximum (VBM) and conduction band minimum (CBM), as illustrated in inset (I) of Fig. 4(e). The Rashba splitting energy was calculated to be ~0.507 meV, with a Rashba coefficient α of ~0.552 eV Å in the valence band maximum regime. These results confirm that strain within the structure induces Rashba splitting, even in materials with inversion symmetry. The presence of heavy elements like Pb in the composition is responsible for stronger relativistic spin-orbit coupling, which along with the broken inversion symmetry leads to such strong Rashba coefficient. One primary repercussion of such Rashba splitting could be perceived on the corresponding charge carrier recombination rate, as the band extrema shifting along the Brillouin zone tunes the excitonic lifetime, as well as the spin texture.

In summary, we synthesized $Cs_2PbI_2Cl_2$ NCs that exhibit sharp excitonic absorption and broad PL at room temperature. MCD measurements reveal significant Zeeman splitting, highlighting robust spin-orbit coupling. The pronounced CD signal below 60 K indicates system asymmetry, while the observed PL peak splitting at lower temperatures and polarization-dependent PL measurements confirm emission anisotropy and Rashba splitting below 70 K. High-resolution synchrotron XRD data shows a transition in unit cell parameters below 70 K, linked to strain induced optical asymmetry and reduced crystal symmetry. Raman frequency modes also undergo transitions around 75 K, supporting the XRD findings. The anharmonic decay model for the A_{1g} mode shows deviation at this temperature, indicating electron-phonon coupling or a structural transition. DFT calculations confirm Rashba spin splitting in the VBM and CBM, aligning with experimental results. Integrating the monolayer-specific Rashba effect within the bulk 2D $Cs_2PbI_2Cl_2$ using chemical strain offers a promising platform for advancing electronic, optoelectronic, and quantum technologies, particularly in spintronics, quantum computing, and photonics. Future studies on $Cs_2PbI_2Cl_2$ nanoplatelets with strain induced asymmetry could explore spin-related phenomena, such as the direct observation of spin-dependent photocurrents and their relationship to symmetry-breaking directions. Investigations using the circular photogalvanic effect could provide deeper insights into spin-orbit coupling and chirality-induced electronic properties. These findings could pave the way for advancements in spintronic devices and optoelectronic applications.

S.K.T. would like to thank UGC for funding and Dr. Pavitra N. Shanbhag for the valuable inputs in structural refinement. R.V. acknowledges the partial support from a SERB-POWER fellowship for this work. T.D. would like to acknowledge DST INSPIRE (DST/INSPIRE/04/2022/003186) for funding. A. Singh and A. Soni would like to acknowledge IIT Mandi for the research facility. Computational work for this study was carried out at the cluster computing facility at Harish Chandra Research Institute. We acknowledge DESY (Hamburg, Germany), a member of the Helmholtz Association HGF, for the provision of experimental facilities. Parts of this research were carried out at P23 *In situ* X-ray Diffraction and Imaging beamline.

[1] A. Rycerz, J. Tworzydło, and C. W. J. Beenakker, Valley filter and valley valve in graphene, Nat. Phys. **3**, 172 (2007).

[2] R. Ahammed and A. De Sarkar, Valley spin polarization in two-dimensional *h*-*M*N (M = Nb, Ta) monolayers: Merger of valleytronics with spintronics, Phys. Rev. B **105**, 045426 (2022).

[3] V. A. Kochelap and V. N. Sokolov, Anisotropic electron transport Rashba effects in valleytronics, Phys. Rev. B **106**, 245422 (2022).

[4] S. Singh, W. Gong, C. E. Stevens, J. Hou, A. Singh, H. Zhang, S. B. Anantharaman, A. D. Mohite, J. R. Hendrickson, Q. Yan, and D. Jariwala, Valley-polarized interlayer excitons in 2D chalcogenide-halide perovskite-van der Waals heterostructures, ACS Nano **17**, 7487 (2023).

[5] Y. P. Shkolnikov, E. P. De Poortere, E. Tutuc, and M. Shayegan, Valley splitting of AlAs two-dimensional electrons in a perpendicular magnetic field, Phys. Rev. Lett. **89**, 226805 (2002).

[6] W. Yao, D. Xiao, and Q. Niu, Valley-dependent optoelectronics from inversion symmetry breaking, Phys. Rev. B **77**, 235406 (2008).

[7] O. Gunawan, Y. P. Shkolnikov, K. Vakili, T. Gokmen, E. P. De Poortere, and M. Shayegan, Valley susceptibility of an interacting two-dimensional electron system, Phys. Rev. Lett. **97**, 186404 (2006).

[8] J. Yin, R. Naphade, P. Maity, L. Gutiérrez-Arzaluz, D. Almalawi, I. S. Roqan, J.-L. Brédas, O. M. Bakr, and O. F. Mohammed, Manipulation of hot carrier cooling dynamics in two-dimensional Dion–Jacobson hybrid perovskites via Rashba band splitting, Nat. Commun. **12**, 3995 (2021).

[9] S. P. Milovanović and F. M. Peeters, Strain controlled valley filtering in multi-terminal graphene structures, Appl. Phys. Lett. **109**, 203108 (2016).

[10] D. Zhang, C. Ge, Y. Wang, Y. Xia, H. Zhao, C. Yao, Y. Chen, C. Ma, Q. Tong, A. Pan, and X. Wang, Enhancing layer-engineered interlayer exciton emission and valley polarization in van der Waals heterostructures via strain, ACS Nano **18**, 17672 (2024).

[11] Z. Guan and S. Ni, Strain-controllable high Curie temperature, large valley polarization, and magnetic crystal anisotropy in a 2D ferromagnetic Janus VSeTe monolayer, ACS Appl. Mater. Interfaces **12**, 53067 (2020).

[12] P. Nagler, M. V. Ballottin, A. A. Mitioglu, F. Mooshammer, N. Paradiso, C. Strunk, R. Huber, A. Chernikov, P. C. M. Christianen, C. Schüller, and T. Korn, Giant magnetic splitting inducing near-unity valley polarization in van der Waals heterostructures, Nat. Commun. **8**, 1551 (2017).

[13] G. Aivazian, Z. Gong, A. M. Jones, R.-L. Chu, J. Yan, D. G. Mandrus, C. Zhang, D. Cobden, W. Yao, and X. Xu, Magnetic control of valley pseudospin in monolayer WSe_2, Nat. Phys. **11**, 148 (2015).

[14] S. Bertrand, J.-M. Parent, R. Côté, and I. Garate, Complete optical valley polarization in Weyl semimetals in strong magnetic fields, Phys. Rev. B **100**, 075107 (2019).

[15] J.-X. Li, W.-Q. Li, S.-H. Hung, P.-L. Chen, Y.-C. Yang, T.-Y. Chang, P.-W. Chiu, H.-T. Jeng, and C.-H. Liu, Electric control of valley polarization in monolayer WSe_2 using a van der Waals magnet, Nat. Nanotechnol. **17**, 721 (2022).

[16] K. F. Mak, K. He, J. Shan, and T. F. Heinz, Control of valley polarization in monolayer MoS_2 by optical helicity, Nat. Nanotechnol. **7**, 494 (2012).

[17] A. Pal, S. Zhang, T. Chavan, K. Agashiwala, C.-H. Yeh, W. Cao, and K. Banerjee, Quantum-engineered devices based on 2D materials for next-generation information processing and storage, Adv. Mater. **35**, 2109894 (2023).

[18] T. Zhang, X. Xu, B. Huang, Y. Dai, and Y. Ma, 2D spontaneous valley polarization from inversion symmetric single-layer lattices, npj Comput. Mater. **8**, 64 (2022).

[19] P. Kumar, T. M. Herath, and V. Apalkov, Ultrafast valley polarization in bilayer graphene, J. Appl. Phys. **130**, 164301 (2021).

[20] S. A. Vitale, D. Nezich, J. O. Varghese, P. Kim, N. Gedik, P. Jarillo-Herrero, D. Xiao, and M. Rothschild, Valleytronics: Opportunities, challenges, and paths forward, Small **14**, 1801483 (2018).

[21] W.-Y. Tong, S.-J. Gong, X. Wan, and C.-G. Duan, Concepts of ferrovalley material and anomalous valley Hall effect, Nat. Commun. **7**, 13612 (2016).

[22] X. Xu, W. Yao, D. Xiao, and T. F. Heinz, Spin and pseudospins in layered transition metal dichalcogenides, Nat. Phys. **10**, 343 (2014).

[23] D. Xiao, G.-B. Liu, W. Feng, X. Xu, and W. Yao, Coupled spin and valley physics in monolayers of MoS_2 and other group-VI dichalcogenides, Phys. Rev. Lett. **108**, 196802 (2012).

[24] J. Chen, K. Wu, W. Hu, and J. Yang, Tunable Rashba spin splitting in two-dimensional polar perovskites, J. Phys. Chem. Lett. **12**, 1932 (2021).

[25] J. Yin, O. M. Bakr, and O. F. Mohammed, Intriguing ultrafast charge carrier dynamics in two-dimensional Ruddlesden–Popper hybrid perovskites, J. Phys. Chem. C **125**, 9630 (2021).

[26] Z. Gan, Y. Cheng, W. Chen, K. P. Loh, B. Jia, and X. Wen, Photophysics of 2D organic–inorganic hybrid lead halide perovskites: Progress, debates, and challenges, Adv. Sci. **8**, 2001843 (2021).

[27] M. T. Pham, E. Amerling, T. A. Ngo, H. M. Luong, K. Hansen, H. T. Pham, T. N. Vu, H. Tran, L. Whittaker-Brooks, and T. D. Nguyen, Strong Rashba-Dresselhaus effect in nonchiral 2D Ruddlesden-Popper perovskites, Adv. Opt. Mater. **10**, 2101232 (2022).

[28] Y. Shao, W. Gao, H. Yan, R. Li, I. Abdelwahab, X. Chi, L. Rogée, L. Zhuang, W. Fu, S. P. Lau, S. F. Yu, Y. Cai, K. P.

Loh, and K. Leng, Unlocking surface octahedral tilt in two-dimensional Ruddlesden-Popper perovskites, Nat. Commun. **13**, 138 (2022).

[29] D. Giovanni, S. Ramesh, M. Righetto, J. W. Melvin Lim, Q. Zhang, Y. Wang, S. Ye, Q. Xu, N. Mathews, and T. C. Sum, The physics of interlayer exciton delocalization in Ruddlesden–Popper lead halide perovskites, Nano Lett. **21**, 405 (2021).

[30] F. Wu, F. Qu, and A. H. MacDonald, Exciton band structure of monolayer MoS_2, Phys. Rev. B **91**, 075310 (2015).

[31] Z. Wang, L. Zhao, K. F. Mak, and J. Shan, Probing the spin-polarized electronic band structure in monolayer transition metal dichalcogenides by optical spectroscopy, Nano Lett. **17**, 740 (2017).

[32] C. M. Gilardoni, F. Hendriks, C. H. van der Wal, and M. H. D. Guimarães, Symmetry and control of spin-scattering processes in two-dimensional transition metal dichalcogenides, Phys. Rev. B **103**, 115410 (2021).

[33] M. H. D. Guimarães and B. Koopmans, Spin accumulation and dynamics in inversion-symmetric van der Waals crystals, Phys. Rev. Lett. **120**, 266801 (2018).

[34] A. Dutta, R. K. Behera, S. Deb, S. Baitalik, and N. Pradhan, Doping Mn(II) in all-inorganic Ruddlesden–Popper phase of tetragonal $Cs_2PbI_2Cl_2$ perovskite nanoplatelets, J. Phys. Chem. Lett. **10**, 1954 (2019).

[35] See Supplemental Material at http://link.aps.org/supplemental/10.1103/PhysRevB.111.L081401 for the details of synthesis of $Cs_2PbI_2Cl_2$ nanoplatelets; characterization and spectroscopic techniques; the Rietveld refined synchrotron x-ray diffraction profiles of $Cs_2PbI_2Cl_2$ and refinement parameters; temperature dependence of cell parameters and Raman modes; XRD and HRTEM of Cs_2PbI_2BrCl; the interplanar distances of $Cs_2PbI_2Cl_2$ and Cs_2PbI_2BrCl; MCD comparison between $Cs_2PbI_2Cl_2$ and $CsPb(Br/Cl)_3$; temperature-dependent steady state PL of $Cs_2PbI_2Cl_2$; W-H plots; and computational methodology, optimized geometry, and band structure plot of $Cs_2PbI_2Cl_2$ (see also Refs. [42–45] therein).

[36] D. Rawat, A. Thomas, A. P. Singh Rana, C. Bera, and A. Soni, Symmetry breaking and structural instability in ultrathin 2H-TaS_2 across the charge density wave transition, Phys. Rev. B **109**, 155411 (2024).

[37] J. Li, Q. Yu, Y. He, C. C. Stoumpos, G. Niu, G. G. Trimarchi, H. Guo, G. Dong, D. Wang, L. Wang, and M. G. Kanatzidis, $Cs_2PbI_2Cl_2$, all-inorganic two-dimensional Ruddlesden–Popper mixed halide perovskite with optoelectronic response, J. Am. Chem. Soc. **140**, 11085 (2018).

[38] P. Acharyya, T. Ghosh, K. Pal, K. Kundu, K. Singh Rana, J. Pandey, A. Soni, U. V. Waghmare, and K. Biswas, Intrinsically ultralow thermal conductivity in Ruddlesden–Popper 2D perovskite $Cs_2PbI_2Cl_2$: Localized anharmonic vibrations and dynamic octahedral distortions, J. Am. Chem. Soc. **142**, 15595 (2020).

[39] K. F. Mak, D. Xiao, and J. Shan, Light–valley interactions in 2D semiconductors, Nat. Photonics **12**, 451 (2018).

[40] G. K. Williamson and W. H. Hall, X-ray line broadening from filed aluminium and wolfram, Acta Metall. **1**, 22 (1953).

[41] N. K. Singh, D. Rawat, D. Dey, A. Elsukova, P. O. A. Persson, P. Eklund, A. Taraphder, and A. Soni, Electron-phonon coupling and quantum correction to topological magnetoconductivity in Bi_2GeTe_4, Phys. Rev. B **105**, 045134 (2022).

[42] Q. A. Akkerman, E. Bladt, U. Petralanda, Z. Dang, E. Sartori, D. Baranov, A. L. Abdelhady, I. Infante, S. Bals, and L. Manna, Fully inorganic Ruddlesden-Popper double Cl-I and triple Cl-Br-I lead halide perovskite nanocrystals, Chem. Mater. **31**, 2182 (2019).

[43] W. Kohn and L. J. Sham, Self-consistent equations including exchange and correlation effects, Phys. Rev. **140**, A1133 (1965).

[44] G. Kresse and J. Furthmüller, Efficient iterative schemes for *ab initio* total-energy calculations using a plane-wave basis set, Phys. Rev. B **54**, 11169 (1996).

[45] P. E. Blöchl, Projector augmented-wave method, Phys. Rev. B **50**, 17953 (1994).